Impingement of filler droplets and weld pool dynamics during gas metal arc welding process

Y. Wang, H.L. Tsai *

Department of Mechanical and Aerospace Engineering and Engineering Mechanics, University of Missouri-Rolla, Rolla, MO 65409, USA

Abstract

A mathematical model and the associated numerical technique have been developed to simulate, for the first time, the dynamic impinging process of filler droplets onto the weld pool in spot gas metal arc welding (GMAW). Filler droplets driven by gravity, electromagnetic force, and plasma arc drag force, carrying mass, momentum, and thermal energy periodically impinge onto the base metal, leading to a liquid weld puddle. Transient weld pool shape and the complicated fluid flow in the weld pool caused mainly by the combined effect of droplet impinging momentum and surface tension are calculated. © 2001 Elsevier Science Ltd. All rights reserved.

1. Introduction

In both gas tungsten arc welding (GTAW) and gas metal arc welding (GMAW), fluid flow in the weld pool can be caused by electromagnetic force, surface tension gradients at the free surface (Marangoni effect), thermal and/or solutal gradients (natural convection), and plasma arc drag force [1]. However, compared to GTAW, GMAW involves impingement of filler droplets onto the weld pool, creating much more complicated transport phenomena in the weld pool [2]. Depending upon surface condition at the free surface, modeling of GTAW process can be generally divided into two categories. In the first category, the free surface was assumed to be flat [3–5]. Lin and Eagar [6] found that when current is below 200 A, the arc pressure has little effect on the flatness of the weld pool surface. In the second category, the depression of free surface was considered [7–9]. Tsai and Kou [10] used pool-surface fitting orthogonal curvilinear coordinates to study the electromagnetic force-induced convection in weld pools with a free surface.

In relation to GMAW research, Simpson and Zhu [11] theoretically studied the formation of molten droplets at a consumable anode and found that the droplet shape for currents under 250 A is close to spherical. Waszink and Graat [12] experimentally investigated different forces acting on the droplet in an arc atmosphere. Heald et al. [13] discussed different droplet transfer modes for an electrode under various current conditions. Tsao and Wu [14] presented a two-dimensional, stationary weld pool convection model by assuming the weld pool surface to be flat. Using boundary-fitted coordinates, Kim and Na [15] presented a three-dimensional quasi-steady heat and fluid flow analysis for the moving heat source of GMAW process with deformed free surface. Recently, Ushio and Wu [16] used a boundary-fitted non-orthogonal coordinate system to handle the largely deformed GMA weld pool surface and predicted the weld dimensions. In their study, however, heat delivered by the droplet was approximated by an internal heat-generation term, and the impact of droplets onto the weld pool was assumed to be a constant force acting on the surface. In other words, the actual droplet impinging process was not simulated. In the study of thermal spray process, Trapaga et al. [17] and Delplanque et al. [18] simulated fluid flow, heat transfer, and solidification for a single molten droplet impinging onto the substrate. However, their studies were limited to a single droplet and no arc energy, as in

* Corresponding author. Tel.: +1-573-341-4945; fax: +1-573-341-4115.

E-mail address: tsai@umr.edu (H.L. Tsai).

Nomenclature

A_v	constant, in Eq. (18)
$\boldsymbol{B}$	magnetic induction vector
B_θ	self-induced azimuthal magnetic field
c	specific heat
c_1	permeability coefficient, defined in Eq. (7)
C	coefficient, defined in Eq. (8)
C_{ds}	drag coefficient, in Eq. (36)
d	dendrite arm spacing
D_d	droplet diameter
f	mass fraction
f^α	sulfur concentration
F	volume of fluid function
F_d	drop frequency
F_{drag}	plasma drag force acting on the droplet
g	volume fraction or gravitational acceleration
h	enthalpy
h_c	convective heat-transfer coefficient between base metal and its surroundings
H	latent heat of fusion
H_w	distance between electrode tip and base metal
H_b	thickness of base metal
H_v	latent heat of vaporization
I	welding current
$\boldsymbol{J}$	current density vector
J_r	radial current density
J_z	axial current density
k	thermal conductivity
K	permeability function, in Eq. (7)
$\vec{n}$	vector normal to the local free surface
p	pressure
p_v	vapor pressure or any other applied external pressure
P_{atm}	atmospheric pressure
q_{conv}	heat loss by convection
q_{evap}	heat loss by evaporation
q_{radi}	heat loss by radiation
$r\text{–}z$	cylindrical coordinate system
R	gas constant
R_b	radius of the base metal
Re	Reynolds number
$\vec{s}$	vector tangential to the local free surface

S_ϕ	source term, in Eq. (40)
t	time
δt	time interval
T	temperature
T_l	liquidus temperature
T_s	solidus temperature
T_∞	ambient temperature
T_0	reference temperature for natural convection
u	velocity in r-direction
u_w	arc voltage
v	velocity in z-direction
v_g	plasma gas velocity
$\boldsymbol{V}$	velocity vector
$\tilde{V}$	calculated temporary velocity vector, in Eq. (41)
$\boldsymbol{V}_r$	relative velocity vector ($= \boldsymbol{V}_1 - \boldsymbol{V}_s$)
W	melt evaporation rate

Greek symbols

β_T	thermal expansion coefficient
γ	surface tension
$\partial\gamma/\partial T$	surface tension temperature gradients
ε	surface radiation emissivity
κ	free surface curvature
μ_l	dynamic viscosity
μ_0	magnetic permeability
η	arc efficiency
η_d	ratio of droplet energy to total arc energy
ϕ	electric potential
σ	Stefan–Boltzmann constant
σ_e	electrical conductivity
σ_c	arc current distribution parameter
σ_q	arc heat flux distribution parameter
ρ	density
τ	viscous stress tensor
$\tau_{\vec{s}}$	Marangoni shear stress, in Eq. (13)

Subscripts

b	base metal
d	droplet
g	plasma gas
l	liquid phase
r	relative to solid phase velocity
s	solid phase

GMAW process, was considered. In summary, so far no mathematical model is available to simulate the dynamic impinging process of filler droplets periodically falling onto the weld pool and the resulting fluid flow and heat transfer in the weld pool.

In this paper, a mathematical model employing the volume of fluid (VOF) technique [19] and the continuum formulation [20] is developed to simulate fluid flow in the weld pool, resulting from the dynamic impinging of droplets onto the weld pool. The VOF technique can handle a transient deformed weld pool surface, while the continuum formulation can handle fusion and solidification for the entire domain including the liquid region, the mush zone, and the solid region. The scope of the study includes the impinging process of the first droplet onto a subcooled base metal and the growth of the weld pool puddle, until the weld pool is completely solidified after the arc is turned off and the last droplet falls.

2. Mathematical model

2.1. Governing equations

Fig. 1 shows a schematic sketch of a stationary axisymmetric GMAW system. It is assumed spherical droplets with uniform initial temperature, zero initial velocity, and at a certain height fall onto the base metal which is initially at room temperature. The droplets driven by gravity, electromagnetic force, and plasma drag force, carrying mass, momentum, and thermal energy impinge onto the base metal at a certain frequency. The base metal will gradually be melted by the plasma arc heat flux and by the thermal energy carried by the droplets. The dimensions of the weld pool increase as more droplets are deposited onto the base metal. For convenience, the mathematical formulation given below is valid for both the base metal and the liquid droplet; however, only the droplet subjects to plasma drag force. Once a droplet reaches the free surface, the droplet is considered to be part of the base metal.

The differential equations governing the conservation of mass, momentum, and energy based on continuum formulation given by Chiang and Tsai [20] are modified and used in the present study. They are given below:

Continuity

$$\frac{\partial}{\partial t}(\rho) + \nabla \cdot (\rho \boldsymbol{V}) = 0. \tag{1}$$

Momentum

$$\frac{\partial}{\partial t}(\rho u) + \nabla \cdot (\rho \boldsymbol{V} u)$$
$$= \nabla \cdot \left(\mu_1 \frac{\rho}{\rho_1} \nabla u \right) - \frac{\partial p}{\partial r} - \frac{\mu_1}{K} \frac{\rho}{\rho_1}(u - u_s)$$
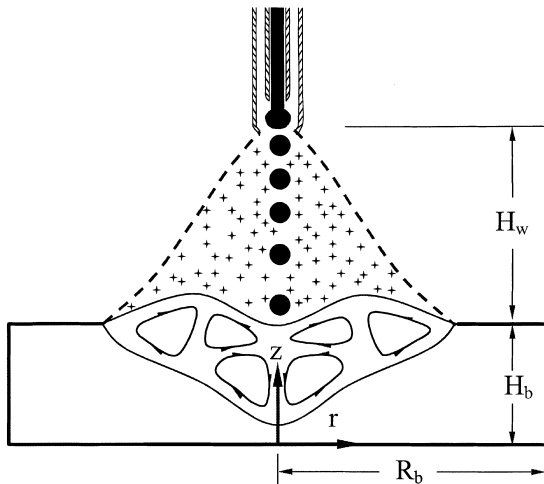

Fig. 1. Schematic sketch of a stationary GMAW system and dimensions of the weld workpiece.

$$- \frac{C\rho^2}{K^{1/2}\rho_1}|u - u_s|(u - u_s) - \nabla \cdot (\rho f_s f_1 \boldsymbol{V}_r u_r)$$
$$+ \nabla \cdot \left(\mu_1 u \nabla \left(\frac{\rho}{\rho_1} \right) \right) + \boldsymbol{J} \times \boldsymbol{B}|_r, \tag{2}$$

$$\frac{\partial}{\partial t}(\rho v) + \nabla \cdot (\rho \boldsymbol{V} v)$$
$$= \rho g + \nabla \cdot \left(\mu_1 \frac{\rho}{\rho_1} \nabla v \right) - \frac{\partial p}{\partial z} - \frac{\mu_1}{K} \frac{\rho}{\rho_1}(v - v_s)$$
$$- \frac{C\rho^2}{K^{1/2}\rho_1}|v - v_s|(v - v_s) - \nabla \cdot (\rho f_s f_1 \boldsymbol{V}_r v_r)$$
$$+ \nabla \cdot \left(\mu_1 v \nabla \left(\frac{\rho}{\rho_1} \right) \right) + \rho g \beta_T (T - T_0) + \boldsymbol{J} \times \boldsymbol{B}|_z + F_{\text{drag}}. \tag{3}$$

Energy

$$\frac{\partial}{\partial t}(\rho h) + \nabla \cdot (\rho \boldsymbol{V} h) = \nabla \cdot \left(\frac{k}{c_s} \nabla h \right) + \nabla \cdot \left(\frac{k}{c_s} \nabla (h_s - h) \right)$$
$$- \nabla \cdot (\rho (\boldsymbol{V} - \boldsymbol{V}_s)(h_1 - h)). \tag{4}$$

Note the physical meanings of each term appearing in the above equations were discussed in [20,21] and will not be repeated here. The similar set of equations has been previously employed by the author to successfully predict the formation of macrosegregation during alloy solidification [21]. In Eqs. (1)–(4), the continuum density, specific heat, thermal conductivity, solid mass fraction, liquid mass fraction, velocity, and enthalpy are defined as follows:

$$\rho = g_s \rho_s + g_1 \rho_1, \quad c = f_s c_s + f_1 c_1,$$
$$k = g_s k_s + g_1 k_1, \quad f_s = \frac{g_s \rho_s}{\rho}, \quad f_1 = \frac{g_1 \rho_1}{\rho}, \tag{5}$$
$$\boldsymbol{V} = f_s \boldsymbol{V}_s + f_1 \boldsymbol{V}_1, \quad h = h_s f_s + h_1 f_1.$$

If the phase specific heat is assumed constant, the phase enthalpy for the solid and the liquid can be expressed as:

$$h_s = c_s T, \quad h_1 = c_1 T + (c_s - c_1) T_s + H, \tag{6}$$

where H is the latent heat of fusion or solidification for the alloy.

The assumption of permeability function in the mushy zone requires consideration of the growth morphology specific to the alloy under study. In the present study, the permeability function analogous to fluid flow in porous media is assumed, employing the Carman–Kozeny equation [22,23]

$$K = \frac{g_1^3}{c_1(1 - g_1)^2}, \quad c_1 = \frac{180}{d^2}, \tag{7}$$

where d is proportional to the dendrite dimension, which is assumed to be a constant and is on the order of

10^{-2} cm. The inertial coefficient, C, in Eqs. (2) and (3), can be calculated from [24]

$$C = 0.13g_l^{-3/2}. \tag{8}$$

It is noted that in Eq. (3), the plasma drag force, F_{drag}, is valid only for the droplet.

2.2. Tracking of solid–liquid interface

The solid/liquid phase-change boundary is handled by the continuum model [20]. The third, fourth, and fifth terms on the right-hand side of Eq. (2) and the fourth, fifth, and sixth terms on the right-hand side of Eq. (3) vanish at the solid phase because $u = u_s = v = v_s = 0$ and $f_l = 0$. Since K goes to infinity due to $g_l = 1$ in Eq. (7) and $f_s = 0$, all the aforementioned terms also vanish for the liquid region. These terms are only valid in the mush zone where $0 < f_l < 1$ and $0 < f_s < 1$. In stationary gas metal arc welding, as arc heat flux is fairly concentrated and the cooling rate of the weld is relatively high (as compared to casting), the mushy zone is expected to be very small. Hence, it is assumed that the solid phase velocity is zero in the mushy zone. As the mushy zone is small in the present study, effects of some terms related to mushy zone (e.g., the third and fourth terms on the right-hand side of Eq. (2)) on weld pool fluid flow may be negligible; and accordingly the equations can be simplified. However, the "complete" equations are presented here which can be easily extended to a three-dimensional welding process in which the size of mushy zone is greater. By using the continuum model, there is no need to explicitly track the phase-change boundaries; and the liquid region, the mush zone, and the solid region all are handled by the same Eqs. (2) and (3). During fusion or the solidification process, the latent heat is absorbed or released in the mush zone, which is handled through the use of enthalpy defined in Eq. (6).

2.3. Tracking of free surface

The algorithm of VOF is used to track the moving free surface [19]. The fluid configuration is defined by a VOF function, $F(r, z, t)$, which tracks the location of free surface. This function represents the VOF per unit volume and satisfies the following conservation equation:

$$\frac{dF}{dt} = \frac{\partial F}{\partial t} + (\mathbf{V} \cdot \nabla)F = 0. \tag{9}$$

When averaged over the cell of a computing mesh, the averaged value of F in a cell is equal to the fractional volume of the cell occupied by fluid. Hence, a unit value of F corresponds to a cell full of fluid, whereas a zero value indicates the cell containing no fluid. The cells with F values between zero and one are partially filled with fluid and are identified as surface cells.

2.4. Boundary conditions

The corresponding boundary conditions for Eqs. (1)–(4) are given below:

2.4.1. Top free surface

For cells containing a free surface, the following pressure condition must be satisfied [19]:

$$p = p_v + \gamma\kappa, \tag{10}$$

where p is the pressure at the free surface in a direction normal to the local free surface, p_v the applied external pressure acting on the free surface which is assumed to be the atmospheric pressure in the present study, and κ is the free surface curvature given by [19]

$$\begin{aligned}
\kappa &= -\left[\nabla \cdot \left(\frac{\vec{n}}{|\vec{n}|}\right)\right] \\
&= \frac{1}{|\vec{n}|}\left[\left(\frac{\vec{n}}{|\vec{n}|} \cdot \nabla\right)|\vec{n}| - (\nabla \cdot \vec{n})\right],
\end{aligned} \tag{11}$$

where $\vec{n}$ is a vector normal to the local free surface which equals the gradient of the VOF function

$$\vec{n} = \nabla F. \tag{12}$$

The effect of arc pressure on the weld pool is ignored, as the current used in the present study is below 200 A [6]. The temperature-dependent Marangoni shear stress at the free surface in a direction tangential to the local free surface is given by [25]

$$\tau_{\vec{s}} = \mu_l \frac{\partial(\mathbf{V} \cdot \vec{s})}{\partial \vec{n}} = \frac{\partial\gamma}{\partial T}\frac{\partial T}{\partial \vec{s}}, \tag{13}$$

where $\vec{s}$ is a vector tangential to the local free surface. The top surface receives electric arc heat flux (which is assumed to be a Gaussian distribution) and dissipates heat to the surroundings through convection, radiation, and metal vaporization via the following formula:

$$k\frac{\partial T}{\partial z} = \frac{\eta(1-\eta_d)Iu_w}{2\pi\sigma_q^2}\exp\left(-\frac{r^2}{2\sigma_q^2}\right) - q_{conv} - q_{radi} - q_{evap}, \tag{14}$$

where I is the welding current, η the arc thermal efficiency, η_d the ratio of droplet energy to the total arc energy, u_w the arc voltage, and σ_q is the arc heat flux distribution parameter. It is noted that in Eq. (14), it is assumed that the arc heat flux impacts perpendicular to the base metal. The heat loss due to convection, radiation, and evaporation can be written as:

$$q_{conv} = h_c(T - T_\infty), \tag{15}$$

$$q_{radi} = \sigma\varepsilon(T^4 - T_\infty^4), \tag{16}$$

$$q_{evap} = WH_v, \tag{17}$$

where H_v is the latent heat for liquid–vapor phase change, and W is the melt mass evaporation rate. For a metal such as steel, W can be written as [26]:

$$\log(W) = A_v + \log P_{atm} - 0.5 \log T, \tag{18}$$

$$\log P_{atm} = 6.121 - \frac{18{,}836}{T}. \tag{19}$$

2.4.2. Bottom surface, $z = 0$

$$-k \frac{\partial T}{\partial z} = q_{conv}, \tag{20}$$

$$u = 0, \quad v = 0. \tag{21}$$

2.4.3. Symmetrical axis, $r = 0$

$$\frac{\partial T}{\partial r} = 0, \tag{22}$$

$$u = 0, \quad \frac{\partial v}{\partial r} = 0. \tag{23}$$

2.4.4. Side surface, $r = R_b$

$$-k \frac{\partial T}{\partial r} = q_{conv}, \tag{24}$$

$$u = 0, \quad v = 0. \tag{25}$$

2.5. Electromagnetic force

In order to solve Eqs. (2) and (3), the term caused by electromagnetic force should be calculated first. Assuming the electric field is quasi-steady-state and the electrical conductivity is constant, the scalar electric potential, ϕ, satisfies the following Maxwell equation [25]:

$$\nabla^2 \phi = \frac{1}{r} \frac{\partial}{\partial r} \left(r \frac{\partial \phi}{\partial r} \right) + \frac{\partial^2 \phi}{\partial z^2} = 0. \tag{26}$$

The required boundary conditions for the solution of Eq. (26) are:

$$-\sigma_e \frac{\partial \phi}{\partial z} = \frac{I}{2\pi\sigma_c^2}$$
$$\times \exp\left(-\frac{r^2}{2\sigma_c^2} \right) \quad \text{at top free surface}, \tag{27}$$

$$\frac{\partial \phi}{\partial z} = 0 \quad \text{at } z = 0, \tag{28}$$

$$\frac{\partial \phi}{\partial r} = 0 \quad \text{at } r = 0, \tag{29}$$

$$\phi = 0 \quad \text{at } r = R_b, \tag{30}$$

where σ_e is the electrical conductivity. After the distribution of electrical potential is solved, the current density in r- and z-directions can be calculated via

$$J_r = -\sigma_e \frac{\partial \phi}{\partial r}, \tag{31}$$

$$J_z = -\sigma_e \frac{\partial \phi}{\partial z}. \tag{32}$$

The self-induced azimuthal magnetic field is derived from Ampere's law via [25]

$$B_\theta = \frac{\mu_0}{r} \int_0^r J_z r \, dr, \tag{33}$$

where μ_0 is the magnetic permeability. Finally, the two components of electromagnetic force in Eqs. (2) and (3) are calculated via

$$\boldsymbol{J} \times \boldsymbol{B}|_r = -J_z B_\theta, \tag{34}$$

$$\boldsymbol{J} \times \boldsymbol{B}|_z = J_r B_\theta. \tag{35}$$

2.6. Plasma drag force

In Eq. (3), the liquid droplet is subject to plasma drag force between the tip of the electrode and the base metal. The plasma drag force, F_{drag}, is obtained by considering plasma as a gas using the following formula [27]:

$$F_{drag} = C_{ds} \frac{1}{2} \rho_g v_g^2 \left(\frac{\pi D_d^2}{4} \right), \tag{36}$$

where C_{ds} is the drag coefficient for a sphere, ρ_g and D_d, respectively, the plasma gas density and droplet diameter, and v_g is the plasma gas velocity. The central arc plasma velocity is assumed to have the same distribution as that in GTAW [28] and can be approximated by the following formula:

$$\frac{v_g}{v_{g\max}} = \frac{27}{4} \left(\frac{z - H_b}{H_w} \right)^2 \left(1 - \frac{z - H_b}{H_w} \right), \tag{37}$$

where $v_{g\max}$ is the maximum velocity, which is assumed to be 50.0 m/s [29], H_w the arc length which is the distance between the tip of the electrode and the base metal, and H_b is the thickness of the base metal.

The drag coefficient depends on the Reynolds number and is given by [27]

$$C_{ds} = \frac{24}{Re} + \frac{6}{\sqrt{1 + Re}} + 0.4 \quad \text{for } 0 < Re$$
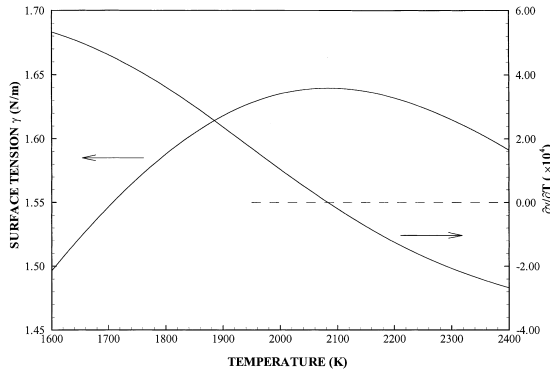$$< 200{,}000 \tag{38}$$

Fig. 2. Surface tension, γ, and its temperature gradients, $\partial\gamma/\partial T$, as a function of temperature for a pseudo-binary Fe–S system, S = 200 ppm. The maximum surface tension occurs at 2085 K.

where $Re = \rho_g v_g D_d / \mu_g$ and μ_g is the plasma gas viscosity. The plasma gas density and viscosity are evaluated at an average plasma gas temperature $T_g = 8000$ K [30].

2.7. Surface tension

Generally, surface tension of a molten weld pool can be a function of temperature and the concentration of some trace element it contains. Due to the availability of experimental data, a binary Fe–S system is selected for the present study. For a pseudo-binary Fe–S system, the surface tension as a function of temperature, T, and sulfur concentration, f^α, is given by [31]

$$\gamma = 1.943 - 4.3 \times 10^{-4}(T - 1723) - RT \times 1.3$$
$$\times 10^{-8} \ln\left(1 + 0.00318 f^\alpha \exp\left(\frac{1.66 \times 10^8}{RT}\right)\right), \quad (39)$$

where R is the gas constant. In the present study, it is assumed that both the filler metal and the base metal contain 200 ppm of sulfur. The surface tension and its temperature gradients are plotted in Fig. 2 as a function of temperature. As shown in the figure, the surface tension increases as temperature increases to a maximum value at about 2085 K and then decreases thereafter. The temperature with maximum surface tension corresponds to the point at which $\partial\gamma/\partial T$ changes its sign from positive to negative.

3. Numerical considerations

The governing differential equations (Eqs. (1)–(4), (9), and (26)) and all related supplemental and boundary conditions were solved through the following iterative scheme:

1. Eq. (26) and the associated boundary conditions were solved and the electromagnetic forces in the r- and z-directions were calculated via Eqs. (34) and (35).

2. Eqs. (1)–(3) and the associated boundary conditions were solved iteratively to obtain velocity and pressure distributions.
3. Eq. (4) was solved for the enthalpy and temperature distribution. Surface tension, in Eq. (39) was updated and iteration was performed between steps 2 and 3 until converged solutions of velocity, pressure, and temperature distributions were achieved.
4. Eq. (9) was solved to obtain the new free surface and domain of the weld pool.
5. Advance to the next time step and back to step 2 until the desired time is reached.

The momentum equations can be cast into the general format suggested by Patankar [32]

$$\frac{\partial(\rho V)}{\partial t} + \nabla \cdot (\rho V V) = \nabla \cdot \tau + S_\phi, \quad (40)$$

where τ is the viscous stress tensor and S_ϕ is the source term, which includes the pressure gradient, the Darcy's function, the relative phase motion, the plasma drag force, and the body force (electromagnetic, gravitational, and buoyancy force) in the momentum equations. Eq. (40) is solved in finite difference form with a two-step projection method. In the first step, the equation was discretized as follows [19]:

$$\frac{\tilde{V} - V^n}{\delta t} = -\nabla \cdot (VV)^n + \frac{1}{\rho^n}\nabla \cdot \tau^n + \frac{1}{\rho^n}S_\phi^n, \quad (41)$$

where the velocity field $\tilde{V}$ is explicitly computed from incremental changes in the field V^n resulting from advection, viscosity, and the source term. In the second step, the velocity field $\tilde{V}$ is projected onto a zero-divergence vector field V^{n+1} using the following two equations:

$$\frac{V^{n+1} - \tilde{V}}{\delta t} = -\frac{1}{\rho^n}\nabla p^{n+1}, \quad (42)$$

$$\nabla \cdot V^{n+1} = 0. \quad (43)$$

These two equations can be combined to become a single Poisson equation for pressure, which is solved by the incomplete Cholesky conjugate gradient (ICCG) solution technique [33]

$$\nabla \cdot \left[\frac{1}{\rho^n}\nabla p^{n+1}\right] = \frac{\nabla \cdot \tilde{V}}{\delta t}. \quad (44)$$

In the solution of Eq. (9), a $\tilde{F}$ was defined via

$$\tilde{F} = F^n - \delta t \nabla \cdot (VF^n). \quad (45)$$

Then, the new fluid domain F^{n+1} can be calculated via a divergence correction to obtain

$$F^{n+1} = \tilde{F} + \delta t(\nabla \cdot V)F^n. \quad (46)$$

Following the MAC scheme [34], the r- and z-velocity components are located at cell face centers on lines of constants r and z, respectively; while the pressure, VOF function, temperature, and the scalar electric potential are located at cell centers.

Since the governing equations are valid for the entire domain including the liquid phase, the solid phase, and the mushy zone, there is no need to track the geometrical shape and the extent of each phase. Hence, a fixed-grid system was used in the numerical calculation. A non-uniform grid system of 90×120 nodes (r- and z-directions) with finer spacing in and near the weld pool domain was utilized for a total computational domain of 18.8×18 mm. Time step size varies in the computer program, but the initial one is 10^{-4} s. Calculations were executed on HP-9000/C200 workstations and the total CPU time for a typical case was about 4 h.

4. Results and discussion

Both the base metal and the filler droplets are assumed to be 304 stainless steel containing 200 ppm of sulfur, and the thermophysical properties for both are summarized in Table 1. For a typical GMAW process, the following welding conditions are assumed [35]: current 155 A; voltage 12 V; wire feed speed 60.0 mm/s; wire diameter 0.89 mm; arc thermal efficiency 80% (i.e., $\eta = 80\%$); and the ratio of droplet energy to the total arc thermal energy 30% (i.e., $\eta_d = 30\%$).

It is assumed that droplets are steadily generated with a diameter of 1.5 mm. By considering the wire feed speed and the diameters of the electrode and the droplet, the frequency of droplet generation is calculated to be about 14 Hz, which is reasonable for a globular or spray metal transfer [36]. By energy balance, the initial droplet

Table 1
Thermophysical properties of 304 stainless steel and welding conditions

Nomenclature	Symbol	Value (unit)
Constant in Eq. (18)	A_v	2.52
Specific heat of solid phase	c_s	700 (J kg^{-1} K^{-1})
Specific heat of liquid phase	c_l	780 (J kg^{-1} K^{-1})
Thermal conductivity of solid phase	k_s	22 (W m^{-1} K^{-1})
Thermal conductivity of liquid phase	k_l	22 (W m^{-1} K^{-1})
Density of solid phase	ρ_s	7200 (kg m^{-3})
Density of liquid phase	ρ_l	6900 (kg m^{-3})
Thermal expansion coefficient	β_T	4.95×10^{-5} (K^{-1})
Radiation emissivity	ε	0.4
Dynamic viscosity	μ_l	0.006 (kg m^{-1} s^{-1})
Latent heat of fusion	H	2.47×10^5 (J kg^{-1})
Magnetic permeability	μ_0	1.26×10^{-6} (H m^{-1})
Solidus temperature	T_s	1670 (K)
Liquidus temperature	T_l	1727 (K)
Ambient temperature	T_∞	293 (K)
Reference temperature	T_0	2400 (K)
Convective heat transfer coefficient	h_c	80 (W m^{-2} K^{-1})
Latent heat of vaporization	H_v	7.34×10^6 (J kg^{-1})
Gas constant	R	8314.3 (J kg^{-1} mole^{-1})
Stefan–Boltzmann constant	σ	5.67×10^8 (W m^{-2} K^{-4})
Electrical conductivity	σ_e	7.14×10^5 (Ω^{-1} m^{-1})
Arc heat flux distribution parameter	σ_q	3.75×10^{-3} (m)
Arc current distribution parameter	σ_c	3.75×10^{-3} (m)
Welding voltage	u_w	12 (V)
Welding current	I	155 (A)
Arc thermal efficiency	η	80%
Ratio of droplet energy to total arc energy	η_d	30%
Atmospheric pressure	P_{atm}	1.013×10^5 (N m^{-2})
Distance between electrode and base metal	H_w	12.0 (mm)
Thickness of base metal	H_b	6.0 (mm)
Radius of base metal	R_b	18.8 (mm)
Initial droplet diameter	D_d	1.5 (mm)
Drop frequency	F_d	14 (Hz)
Initial droplet temperature	T_d	2400 (K)
Plasma gas density	ρ_g	0.06 (kg m^{-3})
Plasma gas viscosity	μ_g	0.00025 (kg m^{-1} s^{-1})

temperature is estimated to be 2400 K, which is of the same order as the anode droplet bulk temperature [12]. It is also assumed that the arc length (between the droplet and the top surface of the base metal) is 12.0 mm [37]. The welding conditions used in the present study are listed in Table 1.

At $t = 0$ s, the first droplet is assumed to detach from the solid electrode in a position 12.0 mm above the base metal. At the same time, the arc energy is turned on. The droplet is accelerated downward by gravity, electromagnetic force, and plasma drag force. There are 14 droplets per second falling onto the base metal until $t = 4.0$ s, when the last droplet is generated and the arc is turned off. In this study, a complete sequence of the impinging process and the resulting weld pool fluid flow from $t = 0.0$ s to $t = 4.0$ s is calculated. However, in the following, results will be presented for the first droplet impinging onto the base metal, for the intermediate stage showing a droplet impinging onto the liquid weld pool, and for the solidification process after the final droplet impinges on the weld pool. Also, in order to increase the readability of the flow pattern in the weld pool, only half of the original grid nodes are used in each velocity vector plot.

Fig. 3 shows a sequence of shapes and positions for the first droplet impinging onto the subcooled base metal. The corresponding velocity profiles are given in Fig. 4. It is seen that the initial spherical droplet is distorted to become elliptical as it approaches the base metal. The electromagnetic force that is inward in the negative r-direction and downward in the negative z-direction causes the change in the droplet shape. The droplet velocity immediately above the base metal is 0.604 m/s, which is similar to the reported experimental value [37] and is greater than 0.47 m/s when only gravity is considered.

As shown in Fig. 4, when the droplet impacts the base metal, liquid flows outward and the droplet becomes flatter. This dynamic phenomenon is similar to that in the thermal spray process [17]. As the droplet contains superheated thermal energy and the base metal is simultaneously heated by the arc heat flux, the droplet does not solidify immediately. In fact, some base metal begins to melt and mix with the droplet, Fig. 3(j). Since the first droplet is not fully solidified before the second one reaches the base metal, a liquid weld pool starts to form immediately after the first droplet.

The mass, momentum, and thermal energy carried by the droplet mix and merge into the base metal. A weld puddle is gradually formed as more droplets deposit onto the weld pool. Fig. 5 shows a sequence of the growth of the weld puddle and the distributions of
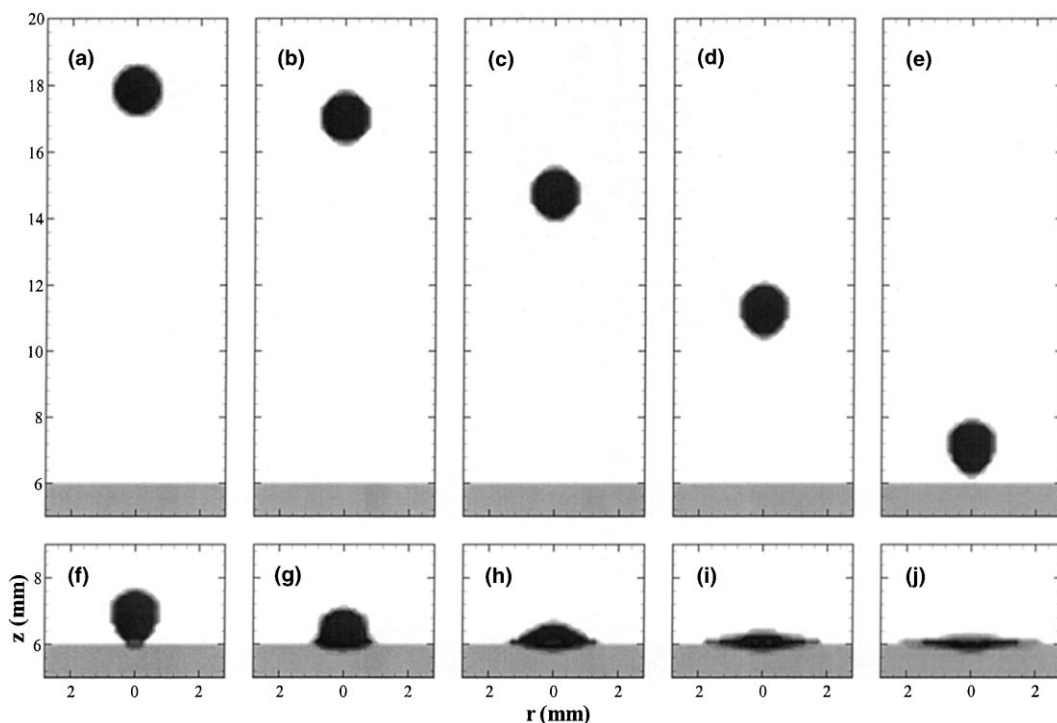

Fig. 3. A sequence of impinging process showing the position and shape of the first droplet falling onto the initially subcooled base metal, initial droplet diameter $D_d = 1.5$ mm, drop frequency $F_d = 14$ Hz, lapsed time between frames $\Delta t = 8.875$ ms for frames (a)–(e) and $\Delta t = 1$ ms for frames (e)–(j).
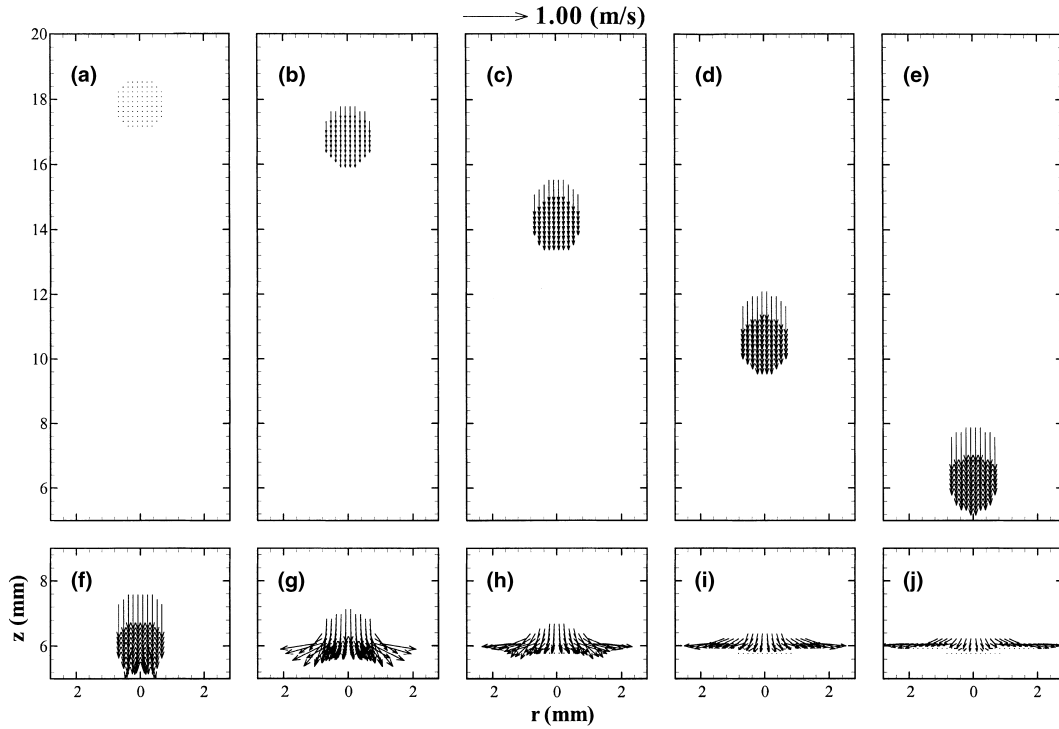
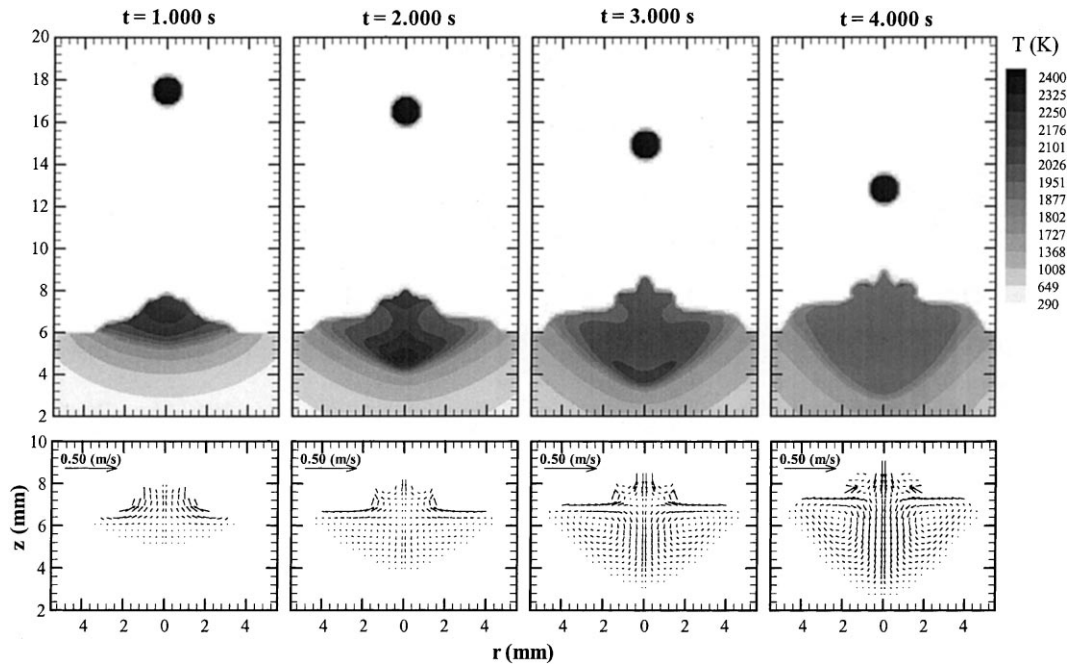Fig. 4. The corresponding velocity profiles for the case as shown in Fig. 3.

Fig. 5. The growth of weld pool puddle and the distributions of temperature and velocity in the weld pool.

temperature and velocity in the weld pool at times 1.0, 2.0, 3.0, and 4.0 s. Note the drop frequency is 14 droplets/s, and the droplets shown at the top of the weld pool at different times are not the same ones. As time increases, more droplets are deposited onto the weld pool and the size of the weld pool, including weld penetration depth, increases.

A typical sequence of the impinging process for a filler droplet onto the weld pool is given in Fig. 6. It is noted that the figures are selected for the instants that will facilitate the following discussion and, hence, the lapsed times between each two figures are not equal. As shown at $t = 3.551$ s, a filler droplet at a higher temperature begins to fall while the weld pool is at a stage caused by the former droplet. At $t = 3.581$ s, the droplet reaches near the top of the free surface with a velocity much greater than the fluid velocities in the weld pool, while the shape of the weld pool has changed and is different from the previous instant. The droplet then impinges onto the weld pool at the top center at $t = 3.586$ s. The downward momentum creates a "crater" in the weld pool at $t = 3.594$ s. Hence, the thermal energy, mass, and momentum carried by the droplet are mixing with the weld pool. It is noted that the droplet's momentum is converted into not only the kinetic energy but also the potential (hydrostatic) energy of the fluid in the wavy weld pool. Also, the increase of the weld pool depth is contributed not only by the impingement of the droplets at a higher temperature, but also by an inward surface flow due to surface tension

force. As the surface temperature near the depressed area in the weld pool is below 2085 K, the maximum surface tension occurs at the center of the weld pool, causing an inward flow at the surface of the pool. The inward flow carries arc thermal energy from the top of the weld pool downward leading to a deep weld penetration. As shown in Fig. 6 at $t = 3.551$ s and $t = 3.594$ s, the fluid near the center of the weld pool is "bounced" back by hydrostatic force and surface tension force, leading to a convex shape of the free surface. After $t = 3.594$ s, another sequence of the droplet impinging process begins with a figure similar to that shown at $t = 3.551$ s.

To study the weld pool dynamics and its solidification process, the arc is turned off and the last droplet is generated at $t = 4.000$ s. Figs. 7 and 8 show, respectively, the temperature and velocity distributions during weld pool solidification. At $t = 4.010$ s, the last droplet just reaches the central top of the weld pool. The droplet sinks to the bottom to form a crater, transforming its kinetic energy into the kinetic and potential (hydrostatic) energy of the weld pool fluid. At $t = 4.018$ s, the concave reaches its lowest position. Due to hydrostatic force, the crater tends to fill up and the weld pool begins to flatten.

At $t = 4.031$ s, the top central fluid has already rebounded and reaches the highest position (the maximum potential energy) at $t = 4.050$ s. As shown in Fig. 8, at $t = 4.050$ s, in regions near the center of the weld pool, the upper portion of the fluid goes up, while the lower
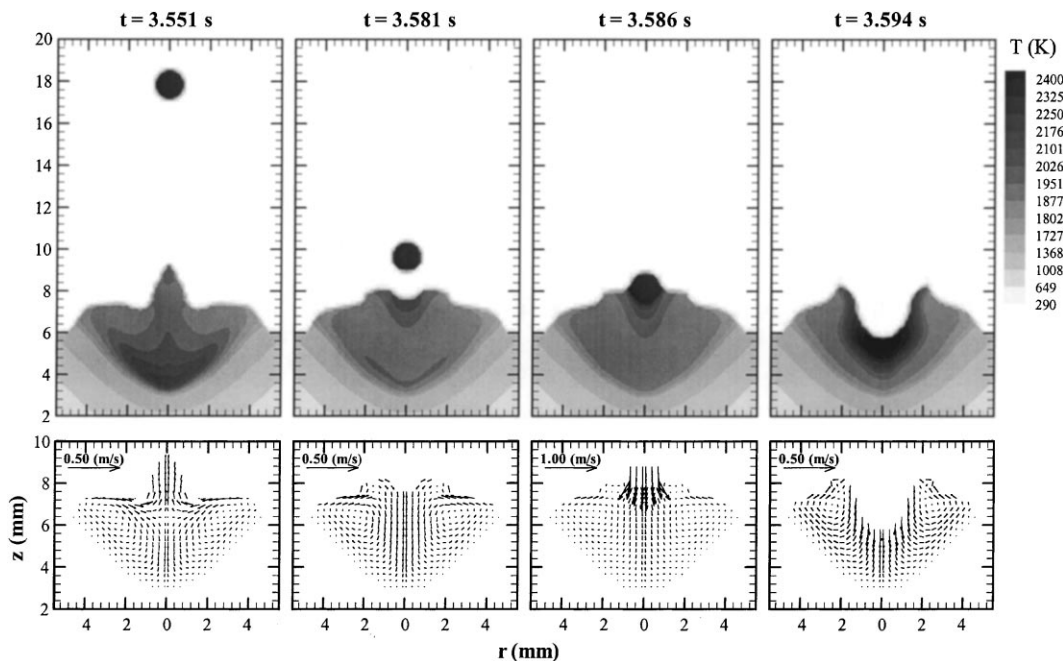

Fig. 6. A sequence of droplet impinging onto the weld pool and the distributions of temperature and velocity in the weld pool.
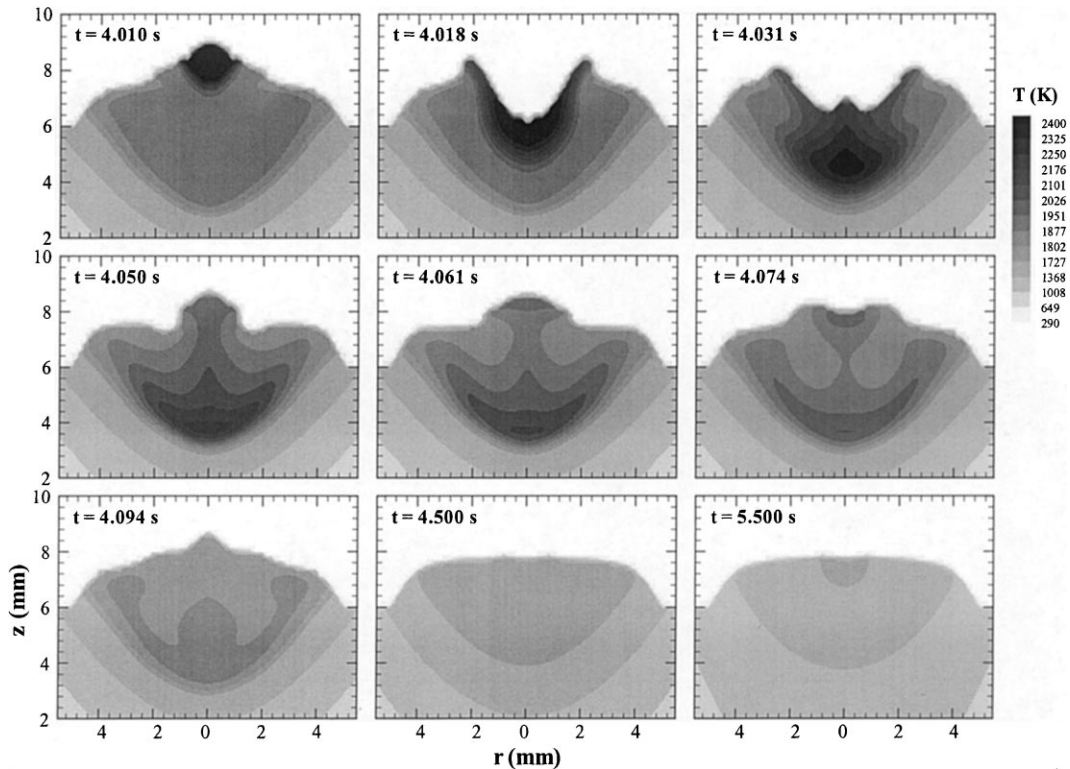
Fig. 7. Weld pool dynamics and temperature distributions at different times after the last droplet was generated and the arc was turned off at $t = 4.0$ s.

portion of the fluid goes down. Under the action of gravity, the fallen fluid, at $t = 4.061$ s, collides with the inward fluid near the surface, resulting in a convex shape which is wider than that at $t = 4.050$ s. At $t = 4.074$ s, the top central surface reaches the lowest level and the fallen fluid results in a much smaller concave than before at $t = 4.018$ s. At $t = 4.094$ s, the top central fluid goes up again similar to, but at a level lower than that at $t = 4.050$ s. Hence, through several times of "up and down" of the weld pool fluid, the momentum carried by the impinged droplets is gradually damped out. From the above discussion, it can be concluded that weld penetration is contributed to mainly by the inward flow due to surface tension (Marangoni effect), as compared to the droplet impinging momentum.

Due to heat loss to the base metal by conduction and to the surroundings by radiation and convection, the size of the molten pool becomes smaller as a result of solidification. At $t = 4.500$ s, the fluid flow in the weld pool is almost diminished, Fig. 8, and the temperature distribution is more uniform than before. At $t = 5.500$ s, the weld pool is completely solidified, and the final shape of the weld bead is similar to the reported experimental results. It is noted that the slight convex of the weld bead is caused by surface tension, and the degree of convexity

depends on the size of the weld bead and the magnitude of the surface tension.

As indicated in [19], some abnormal velocities were found to occur in a number of nodes near the free surface when using the VOF technique. However, it appears that the abnormal velocities do not affect the overall prediction of the velocity distributions. As spatter phenomena are frequently observed in spot GMAW at high currents, special attention was paid in the numerical simulation to see if spatter does occurs. In the calculated results, some very small metal "particles" present above and near the free surface were found, as shown in Fig. 9. It is noted that although these very small particles appear in the temperature plot, they are too small to be shown in the VOF plot. Although theoretically the VOF technique can catch these small particles if a very fine grid system is used, it is not certain if the small metal particles are caused by droplet spatter or by accumulated numerical errors.

On the other hand, it was also observed that the value of VOF function, F in Eq. (9), is not equal to one everywhere within the fluid (e.g., 0.995). In other words, several very small voids exist in the weld pool, Fig. 9. These voids are not shown in the temperature plot, because the temperatures are similar to the surrounding
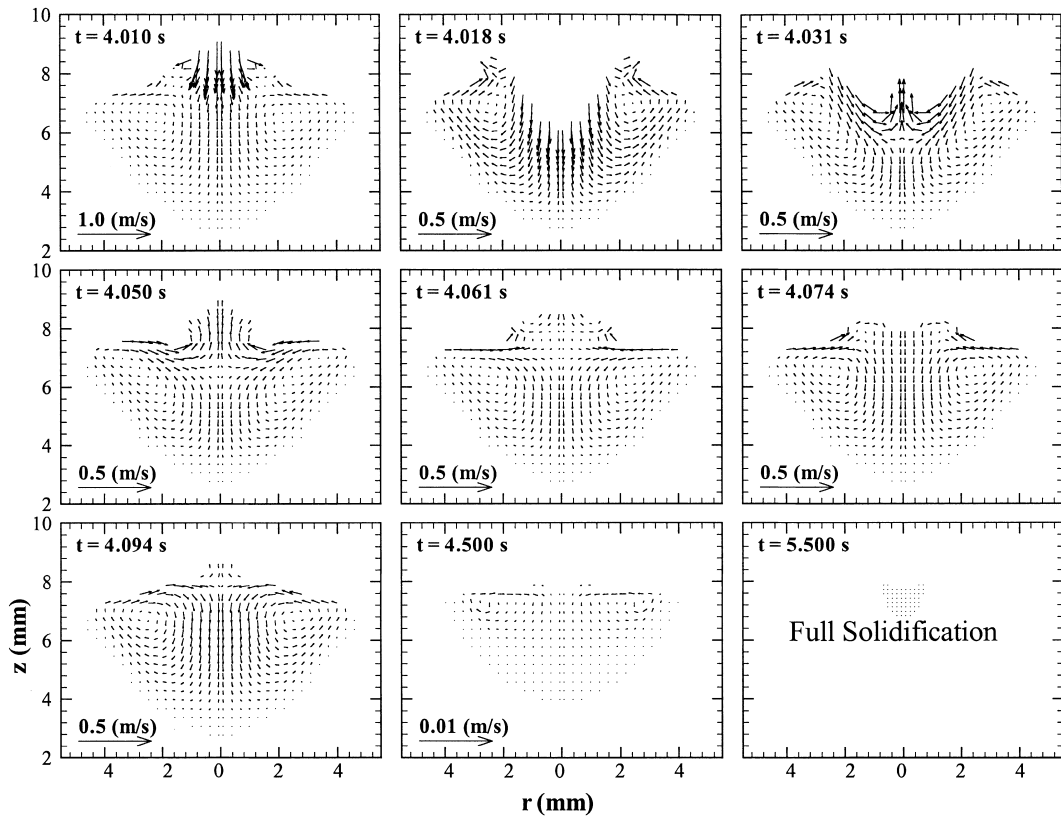
Fig. 8. The corresponding velocity distributions for the case as shown in Fig. 7.
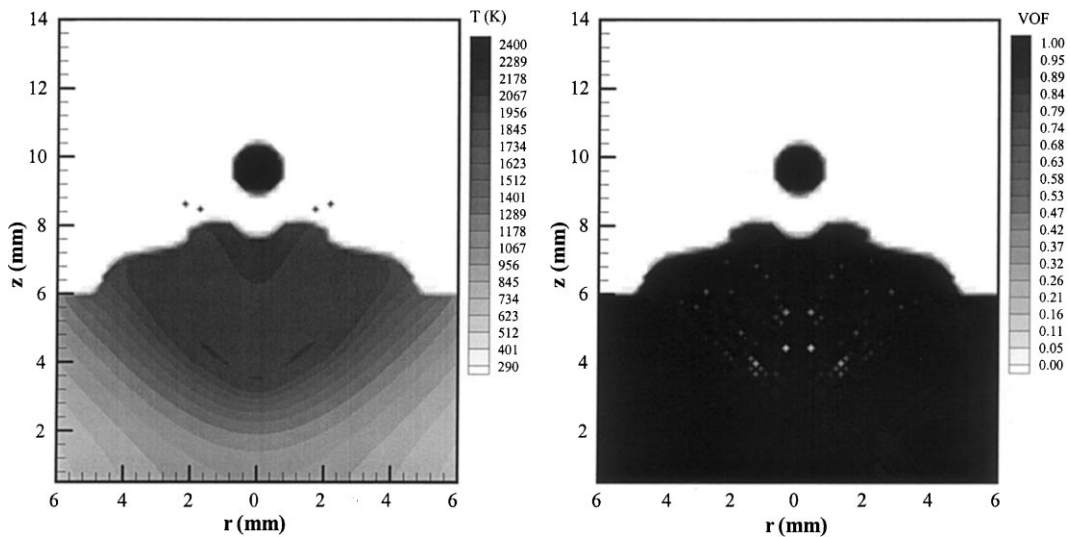

Fig. 9. A figure used as an example for discussing the existence of metal ''particles'' above the weld pool and ''voids'' in the weld pool.

metals. In order to determine possible causes for the formation of voids in the weld pool, several numerical experiments have been conducted. When an exact square

shape of droplets (instead of spherical) were used, almost no void was found in the weld pool. Hence, the voids in the weld pool are caused, at least partially, by

the fact that the rectangular grids used in the present study do not "fit" perfectly with the spherical droplet. As a result, the voids contained in the grids at the edge of the spherical droplet were carried down to the weld pool. It is, therefore, concluded that the voids in the weld pool are caused, at least partially, by numerical errors due to an imperfect fit between the grid system and the spherical droplet.

By the end of the simulation ($t = 4.0$ s), the total released droplet mass is about 5% greater than the mass increased in the weld pool. The accumulation of numerical errors, spatter, metal vaporization, or a combination during the welding process can cause this. In Figs. 5–7, all aforementioned very small metal "particles" were removed. In any case, the simulated results are felt to be reasonable, although strictly controlled experimental results under similar welding conditions are unavailable for comparison.

5. Conclusions

A mathematical model has been developed to simulate the impinging process of filler droplets onto the weld pool and the weld pool dynamics in GMAW process. The VOF technique was used to handle the free surface, while melting and solidification were handled by the continuum formulation. The dimensions and size of the weld puddle were calculated as a function of time. Complicated fluid flow velocity and temperature distributions in the weld pool caused by the combination of droplet impinging momentum, electromagnetic force, surface tension, and gravity were calculated. For stationary GMAW, the droplet impinging momentum is converted to kinetic and potential energy of the fluid in the weld pool and is finally damped out, while the weld penetration is caused mainly by the surface tension force (Marangoni effect).

Acknowledgements

References

[1] J. Szekely, Transport phenomena in welds with emphasis on free surface phenomena, in: S.A. David, J.M. Vitek (Eds.), Recent Trends in Welding Science and Technology, TWR'89, ASM International, 1990, pp. 3–10.

[2] W.G. Essers, R. Walter, Heat transfer and penetration mechanisms with GMA and plasma–GMA welding, Weld. J. (February 1981) 37s–42s.

[3] G.M. Oreper, T.W. Eagar, J. Szekely, Convection in arc weld pools, Weld. J. (November 1983) 307s–312s.

[4] S. Kou, Y.H. Wang, Weld pool convection and its effect, Weld. J. (March 1986) 63s–70s.

[5] R.T.C. Choo, J. Szekely, The effect of gas shear stress on Marangoni flows in arc welding, Weld. J. (September 1991) 223s–233s.

[6] M.L. Lin, T.W. Eagar, Influence of arc pressure on weld pool geometry, Weld. J. (1985) 163s–169s.

[7] T. Zacharia, A.H. Eraslan, K.K. Aidun, Modeling of autogenous welding, Weld. J. 67 (March 1988) 53s–62s.

[8] T. Zacharia, A.H. Eraslan, K.K. Aidun, Modeling of non-autogenous welding, Weld. J. 67 (January 1988) 18s–27s.

[9] R.T.C. Choo, J. Szekely, R.C. Westhoff, Modeling of high current arcs with emphasis on free surface phenomena in the weld pool, Weld. J. 69 (1990) 346s–361s.

[10] M.C. Tsai, S. Kou, Electromagnetic-force-induced convection in weld pools with a free surface, Weld. J. (June 1990) 241s–246s.

[11] S.W. Simpson, P. Zhu, Formation of molten droplets at a consumable anode in an electric welding arc, J. Phys. D: Appl. Phys. 28 (1995) 1594–1600.

[12] J.H. Waszink, L.H.J. Graat, Experimental investigation of the forces acting on a drop of weld metal, Weld. J. (June 1983) 108s–116s.

[13] P.R. Heald, R.B. Madigan, T.A. Siewert, S. Liu, Mapping the droplet transfer modes for an ER100S-1 GMAW electrode, Weld. J. (February 1994) 38s–44s.

[14] M.C. Tsao, C.S. Wu, Fluid flow and heat transfer in GMA weld pools, Weld. J. (March 1988) 70s–75s.

[15] J.W. Kim, S.J. Na, A study on the three-dimensional analysis of heat and fluid flow in gas metal arc welding using boundary-fitted coordinates, Trans. ASME, J. Eng. Ind. 116 (1994) 78–85.

[16] M. Ushio, C.S. Wu, Mathematical modeling of three-dimensional heat and fluid flow in a moving gas metal arc weld pool, Metall. Trans. 28B (1997) 509–516.

[17] G. Trapaga, E.F. Matthys, J.J. Valencia, J. Szekely, Fluid flow heat transfer and solidification of molten metal droplets impinging on substrates: comparison of numerical and experimental results, Metall. Trans. 23B (1992) 701–718.

[18] J.P. Delplanque, E.J. Lavernia, R.H. Rangel, Simulation of micro-pore formation in spray deposition process, in: Transport Phenomena in Materials Processing and Manufacturing ASME HTD-336/FED-240, 1996, pp. 275–282.

[19] D.B. Kothe, R.C. Mjolsness, M.D. Torrey, Ripple: a computer program for incompressible flows with free surfaces, LA-12007-MS, Los Alamos National Laboratory, 1991.

[20] K.C. Chiang, H.L. Tsai, Shrinkage-induced fluid flow and domain change in two-dimensional alloy solidification, Int. J. Heat Mass Transfer 35 (1992) 1763–1769.

[21] Q.Z. Diao, H.L. Tsai, Modeling of solute redistribution in the mushy zone during solidification of aluminum–copper alloys, Metall. Trans. 24A (1993) 963–973.

[22] P.C. Carman, Fluid flow through granular beds, Trans. Inst. Chem. Eng. 15 (1937) 150–166.

[23] K. Kubo, R.D. Pehlke, Mathematical modeling of porosity formation in solidification, Metall. Trans. 16B (1985) 359–366.

[24] G.S. Beavers, E.M. Sparrow, Non-Darcy flow through fibrous porous media, J. Appl. Mech. 36 (1969) 711–714.

[25] R.T.C. Choo, J. Szekely, S.A. David, On the calculation of the free surface temperature of gas–tungsten-arc weld pools from first principles: Part II. Modeling the weld pool and comparison with experiments, Metall. Trans. 23B (1992) 371–384.

[26] T. Zacharia, S.A. David, J.M. Vitek, Effect of evaporation and temperature-dependent material properties on weld pool development, Metall. Trans. 22B (1991) 233–241.

[27] H. Schlichting, Boundary-Layer Theory, sixth ed., McGraw-Hill, New York, 1968 (Chapter I).

[28] S.Y. Lee, S.J. Na, A numerical analysis of a stationary gas tungsten welding arc considering various electrode angles, Weld. J. (September 1996) 269s–279s.

[29] Y.S. Kim, T.W. Eagar, Analysis of metal transfer in gas metal arc welding, Weld. J. (June 1993) 269s–278s.

[30] S. Rhee, E. Kannatey-Asibu Jr., Observation of metal transfer during gas metal arc welding, Weld. J. (October 1992) 381s–386s.

[31] P. Sahoo, T. DeBroy, M.J. Mcnallan, Surface tension of binary metal-surface active solute systems under conditions relevant to welding metallurgy, Metall. Trans. 19B (1988) 483–491.

[32] S.V. Patankar, Numerical Heat Transfer and Fluid Flow, Hemisphere, New York, 1980, pp. 96–102.

[33] D.S. Kerhaw, The incomplete Cholesky-conjugate gradient method for the interactive solution of systems of linear equations, J. Comput. Phys. 26 (1978) 43–65.

[34] J.E. Welch, F.H. Harlow, J.P. Shannon, B.J. Daly, The MAC method: A computing technique for solving viscous, incompressible, transient fluid-flow problems involving free surface, Los Alamos Scientific Laboratory Report LA-3425, 1966.

[35] J.N. DuPont, A.R. Marder, Thermal efficiency of arc welding process, Weld. J. (December 1995) 406s–416s.

[36] S. Liu, T.A. Siewert, Metal transfer in gas metal arc welding: droplet rate, Weld. J. (February 1989) 52s–58s.

[37] J.H. Waszink, M.J. Piena, Experimental investigation of drop detachment and drop velocity in GMAW, Weld. J. (November 1986) 289s–298s.